Air-stable droplet interface bilayers on oil-infused surfaces

Jonathan B. Boreyko[a], Georgios Polizos[b], Panos G. Datskos[b], Stephen A. Sarles[c,1], and C. Patrick Collier[a,1]

[a]Center for Nanophase Materials Sciences, [b]Energy and Transportation Science Division, Oak Ridge National Laboratory, Oak Ridge, TN 37831; and [c]Department of Mechanical, Aerospace, and Biomedical Engineering, University of Tennessee, Knoxville, TN 37996

Edited by Joanna Aizenberg, Harvard University, Cambridge, MA, and accepted by the Editorial Board April 14, 2014 (received for review January 11, 2014)

Droplet interface bilayers are versatile model membranes useful for synthetic biology and biosensing; however, to date they have always been confined to fluid reservoirs. Here, we demonstrate that when two or more water droplets collide on an oil-infused substrate, they exhibit noncoalescence due to the formation of a thin oil film that gets squeezed between the droplets from the bottom up. We show that when phospholipids are included in the water droplets, a stable droplet interface bilayer forms between the noncoalescing water droplets. As with traditional oil-submerged droplet interface bilayers, we were able to characterize ion channel transport by incorporating peptides into each droplet. Our findings reveal that droplet interface bilayers can function in ambient environments, which could potentially enable biosensing of airborne matter.

nanofabrication | superhydrophobic | networks

Inspired by the pitcher plant (1), it was recently found that nano/microstructured hydrophobic substrates can be impregnated with lubricating fluids to create slippery surfaces for droplets (2–5). In contrast to dry, superomniphobic surfaces (6), lubricant-infused surfaces demonstrate stable liquid repellency at extreme pressures and temperatures (5, 7), are self-healing to mechanical damage (5), and their wettability and optical properties can be tuned (7, 8). A wide variety of applications are being explored for lubricant-infused surfaces, such as enhancing condensation heat transfer (9, 10), self-cleaning (11), fog harvesting (12), and omniphobic textiles (13), or minimizing ice nucleation (14, 15), ice adhesion (16, 17), and biofouling (18). Though previous studies have characterized the dynamics and possible wetting states of isolated droplets on lubricant-infused surfaces (5, 19–22), the interactive behavior of multiple droplets has not been reported.

For the more traditional scenario of water droplets completely submerged in a reservoir of immiscible fluid, the physics of droplet–droplet interactions are well known. Water droplets submerged in crude oil can exhibit stable noncoalescence; this is because the crude oil contains surface-active components, such as resins and asphaltenes, which congregate at the droplet interfaces (23). When amphiphilic phospholipids are introduced into an oil reservoir containing water droplets, droplet interface bilayers (DIBs) can form between adjacent water droplets (24, 25). Recently, DIBs have emerged as an ideal model membrane system due to attractive features such as durability (26, 27), tunable size and curvature (28–30), deformability (31), facile electrical characterization of ion channels (32–35), the option to introduce asymmetry into the system (36), and droplet interchangeability (26, 32). In the absence of any stabilizing agents, water droplets colliding in an immiscible fluid will exhibit coalescence when their interaction time exceeds the time required to drain the film of fluid trapped between the droplets (37, 38). Droplet collision is typically controlled by applying a constant force (i.e., gravity) (39, 40), constant approach velocity (41, 42), or constant flow rate (43, 44). For experimental studies in pure oil baths, the time required for colliding water droplets to exhibit film rupture and coalesce typically ranges from 10^{-3} to 10^{2} s, depending on parameters such as oil viscosity, droplet size, and the flow field (40, 42–44).

Here, we show that water droplets in an ambient environment exhibit noncoalescence when colliding on an oil-infused surface, even in the absence of any surfactants. This phenomenon is due to the oil meniscus that surrounds each water droplet; when the oil menisci of neighboring droplets overlap, the menisci spontaneously merge together to minimize their surface energies and an oil film is squeezed upward to form a barrier between the colliding droplets. Though droplet coalescence will eventually occur due to film drainage, the time required for film rupture is several hours for moderate-viscosity [~100 centistokes (cSt)] oils and is 1–3 orders of magnitude longer compared with droplets submerged in an oil bath (40, 42–44). These findings should refine the understanding of using oil-infused substrates for processes involving droplet–droplet interactions, such as condensation (9, 10) and fog harvesting (12).

When incorporating amphiphilic phospholipids into the water droplets, we demonstrate that the thinning oil membrane between noncoalescing droplets gets replaced by a stable lipid bilayer, somewhat analogous to the formation of a black lipid membrane in an aperture painted with oil (45). To our knowledge, this is the first report of producing droplet interface bilayers in an ambient environment. We show that air-stable DIBs still allow for the robust electrical characterization of ion channels inserted in the lipid bilayer. Previously, it has been demonstrated that black lipid membranes or DIBs can be used for biosensing (46–50), light sensing (26), microscale biobatteries (26), electrical circuits (51, 52), and engineering tissue-like material (53). However, these suspended lipid bilayers have always been confined to fluid reservoirs (25, 45). We suggest that our air-stable DIBs will allow for an unprecedented degree of control regarding the fabrication, manipulation, transportation, and utilization of functional droplet networks.

Results and Discussion

Noncoalescence of Water Droplets on Oil-Infused Surfaces. Droplet–droplet interactions were characterized on an oil-infused

Significance

By suspending a lipid bilayer in an aperture or between water droplets, single-molecule transport through membrane channels can be electrically detected. To date, all suspended bilayers have been confined to fluid reservoirs. This study demonstrates that droplet interface bilayers can be created in an ambient environment using noncoalescing water droplets on an oil-infused surface. Air-stable droplet interface bilayers are easy to manipulate and electrically characterize, and could potentially allow for the biosensing of airborne molecules.

Author contributions: J.B.B., S.A.S., and C.P.C. designed research; J.B.B., S.A.S., and C.P.C. performed research; G.P. and P.G.D. contributed new reagents/analytic tools; J.B.B., S.A.S., and C.P.C. analyzed data; and J.B.B. wrote the paper.

The authors declare no conflict of interest.

This article is a PNAS Direct Submission. J.A. is a guest editor invited by the Editorial Board.

[1]To whom correspondence may be addressed. E-mail: colliercp@ornl.gov or ssarles@utk.edu.

This article contains supporting information online at www.pnas.org/lookup/suppl/doi:10.1073/pnas.1400381111/-/DCSupplemental.

superhydrophobic surface. Listed in order of increasing viscosity, the five different oils used for experiments were hexadecane; Krytox 100; 50- and 350-cSt silicone oil (at 25 °C); and Fomblin 25/6 (*SI Appendix*, Table S1). These low surface-tension oils uniformly impregnate the surface roughness to prevent deposited water droplets from directly contacting the substrate: $\theta_{os(a)} \approx \theta_{os(w)} \approx 0°$, where subscripts a, o, and w are the air, oil, and water phases, and s is the substrate (5, 21). The superhydrophobic surface was composed of silicon nanopillars, because it was previously found that nanotextured surfaces are best suited for locking in a film of oil that is long-lasting (54) and highly stable against external forces (55). When a water droplet was deposited onto an oil-infused surface, an oil meniscus rapidly formed around the droplet to balance its three-phase contact line: $\vec{\gamma}_{oa} + \vec{\gamma}_{wo} + \vec{\gamma}_{wa} = 0$. It should be noted that because $\gamma_{wo} + \gamma_{oa} < \gamma_{wa}$ for all oils used here (except hexadecane; *SI Appendix*, Table S2), a thin film of oil is cloaked about the water–air interface, and $\vec{\gamma}_{wa}$ is actually replaced by $\vec{\gamma}_{wo} + \vec{\gamma}_{oa}$ (21, 56). For brevity, the oil-cloaked droplet interface will henceforth be referred to simply as the water–air interface.

When two water droplets came into contact on an oil-infused surface, they exhibited either coalescence or noncoalescence depending on their initial point of contact (Fig. 1). Droplets colliding at the water-air interfaces experienced immediate coalescence, revealing that the thin cloak of oil surrounding the droplets is not sufficient to prevent coalescence (Fig. 1*A*). This scenario will not be considered any further, because the dynamics of conventional droplet coalescence have been reported elsewhere (57). When the initial contact occurred at the droplets' surrounding oil menisci, however, the droplets exhibited noncoalescence for minutes or even hours despite becoming firmly attached to each other (Fig. 1 *B*–*D*).

The mechanism for noncoalescence is a thin film of oil that gets squeezed upward between the droplets as the menisci merge. Surface-tension measurements of the oil–water interfaces confirmed that all of the oils (except for Fomblin) did not contain any appreciable surface-active materials (*SI Appendix*, Fig. S1), indicating that noncoalescence occurs independently of any stabilizing agents. It has previously been shown that water condensing in an oil bath exhibits an ordered hexagonal structure due to delayed coalescence (58); however, without a supporting substrate, these condensate drops were primarily submerged beneath the oil surface, whereas the noncoalescing droplets observed here are suspended almost entirely above the oil interface.

By varying the amount of excess oil on the surface, the contact angle of a deposited droplet and the shape of its oil meniscus could be tuned to control the occurrence of coalescence vs. noncoalescence (*SI Appendix*, Fig. S2). In short, noncoalescence will occur if the oil menisci extend beyond the droplet profiles, which is the case if either of the following conditions are met:

$$\theta_w < 90°, \quad \theta_w > 90° \text{ and } R < L + L_o, \qquad [1]$$

where θ_w is the contact angle of the water droplet on the oil-infused surface (with respect to the horizontal), R is the droplet's radius of curvature, L is the droplet's contact radius with the oil meniscus, and L_o is the decay length of the oil meniscus (*SI Appendix*, Fig. S3). Over hundreds of trials, Eq. **1** was confirmed for a variety of droplet sizes (2.5–10 μL) and oil viscosities (~1–1,000 mPa·s). The cutoff point is illustrated in Fig. 1, where droplets exhibited coalescence for an oil film spin-coated at 1,000 rpm for 45 s (Fig. 1*A*) and noncoalescence for a thicker

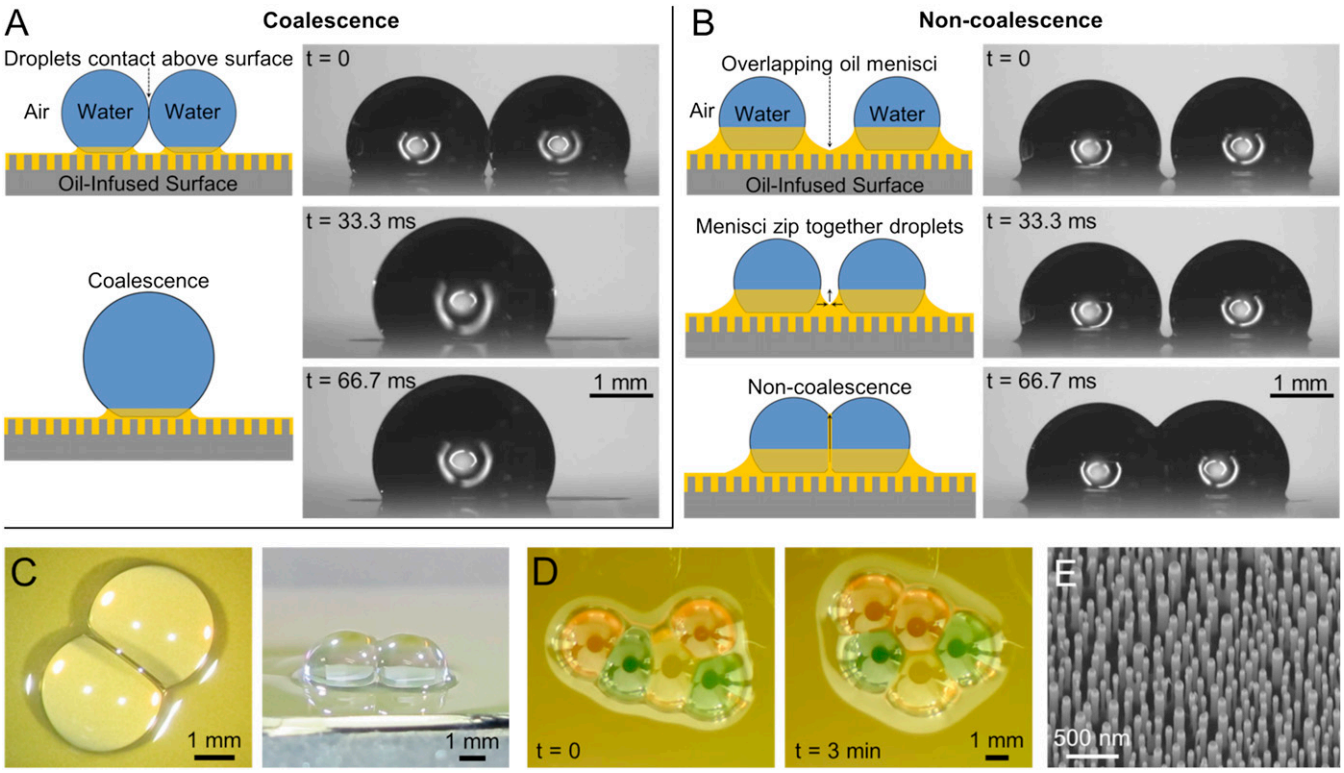

Fig. 1. Interactive behavior of water droplets on an oil-infused surface. (*A*) Droplets colliding at the liquid–air interfaces exhibited coalescence. (*B*) When the oil menisci of two droplets overlapped, an oil film formed between the droplets to enable noncoalescence. (*C*) Top-down and isometric photographs of noncoalescing droplets. (*D*) Multiple droplets could be connected into a network; due to the negligible hysteresis, these networks spontaneously rearranged over time to minimize their surface energy. (*E*) SEM of nanopillared substrate. The oils used were (*A* and *B*) Krytox 100 and (*C* and *D*) Fomblin 25/6; food coloring was used in *D*. See *SI Appendix*, Movies S1–S3.

film spin-coated at 500 rpm for 45 s (Fig. 1*B*). For the remainder of the experiments reported here, an excess oil thickness of ~50 ± 10 μm was deposited over the infused nanostructure; this was chosen because 50 μm of excess oil is thick enough to ensure that the criteria for noncoalescence will consistently be met ($\theta_w \approx 90°$) but is also thin enough to elevate the majority of the water droplet(s) above the oil–air interface.

When the oil menisci of multiple droplets overlap, the droplets spontaneously pull together to minimize the surface energies of the oil menisci. The collision velocity of the droplets is proportional to the viscous-capillary velocity (57) of the oil,

$$v \propto \frac{\gamma_{oa}}{\mu_o}, \qquad [2]$$

where v is the maximum cumulative velocity exhibited by the droplets before deceleration and γ_{oa} and μ_o are the surface tension and viscosity of the oil menisci pulling the droplets together (*SI Appendix*, Fig. S4). When Eq. **1** is satisfied, the water droplets exhibit noncoalescence upon collision due to the formation of an intermediate oil film. After collision, the immobilized droplets remain stuck together and exhibit a near-constant profile over time (the surface was cooled to the dew point to prevent droplet evaporation).

Thin Film Drainage Between Water Droplets. After a period that ranges from seconds to hours depending on the experimental conditions, the intermediate oil film collapses, causing the droplets to finally coalesce together. The drainage time required for film rupture depended primarily upon the viscosity of the oil, with t_c ~10–1,000 s for μ_o ~10 mPa·s and t_c ~1,000–10,000 s for μ_o ~100 mPa·s (Fig. 2). These lifetimes of noncoalescence are 1–3 orders of magnitude longer compared with submerged water droplets (~1 mm) colliding in an oil bath, where t_c ~0.1–10 s for μ_o ~ 10 mPa·s and t_c ~10–100 s for μ_o ~100 mPa·s (40, 42, 44). When an oil containing surfactants is used (Fomblin), the noncoalescing droplets were stable for at least 24 h in the absence of evaporation (*SI Appendix*, Fig. S5).

In addition to oil viscosity, the volume of the colliding water droplets also affected the lifetime of noncoalescence, particularly for the low-viscosity Krytox oil. The tested droplet volumes were 2.5, 5, and 10 μL. The 2.5-μL droplets consistently exhibited shorter droplet lifetimes compared with the 5-μL droplets; this is because droplets with a smaller radius of curvature exhibit a larger Laplace pressure. It would therefore be expected that the 10-μL droplets would last even longer than the 5-μL droplets; however, this was not always the case. The 10-μL droplets exhibited the widest range of noncoalescence lifetimes, with some coalescing almost immediately while others did indeed last longer than the 5-μL droplets. One possible explanation is that larger droplets collide at larger Weber numbers ($We = \rho_w v^2 R/\gamma_{wo}$), which could reduce the initial film thickness. For example, droplet collisions on Krytox oil exhibited We ~0.001 for 2.5-μL droplets compared with We ~0.01 for 10-μL droplets. The importance of inertial effects is attested by the observation that droplets colliding with externally imposed velocities exhibited higher rates of early film rupture compared with static droplets joined together solely by the oil menisci's surface tension.

The drainage and eventual collapse of the oil film is primarily due to the Laplace pressure and long-range intermolecular forces acting on the film (37),

$$\Delta P = \frac{2\gamma_{wa}}{R} + \frac{A_H}{6\pi H(r,t)^3}, \qquad [3]$$

where ΔP is the pressure difference between the droplets and oil film, R is the radius of curvature of two same-sized droplets, A_H is the Hamaker constant, and $H(r,t)$ is the thickness of the oil film. The droplets used here were smaller than the capillary length, $\kappa^{-1} = \sqrt{\gamma_{wa}/\rho g} \approx 3$ mm (4), so gravity is not expected to play a significant role. Because the intermolecular forces scale with H^{-3}, the oil film rapidly collapses as intermolecular forces become dominant at a critical thickness (37, 38),

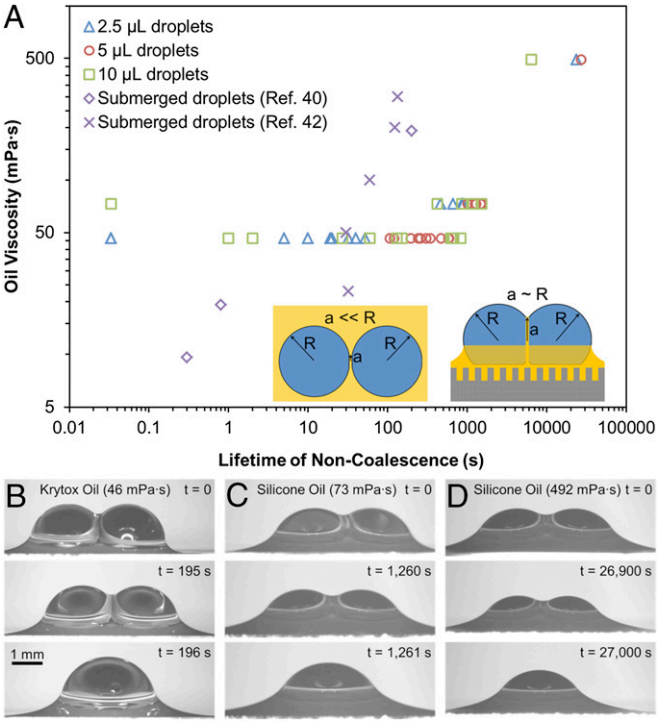

Fig. 2. (*A*) Time required to drain an oil film between water droplets on surfaces infused with Krytox or silicone oils. The substrate was held at 8 °C to prevent droplet evaporation. The drainage time was 1–3 orders of magnitude longer compared with droplets submerged in oil baths (whose data are shown here from refs. 40 and 42), most likely due to the larger film radius (*Inset*). (*B–D*) Side-view imaging of the lifetime of noncoalescing 5-μL droplets on surfaces infused with (*B*) Krytox, (*C*) 50 cSt silicone oil, and (*D*) 350 cSt silicone oil. See *SI Appendix*, Movies S4 and S5.

$$H_c \sim \left(\frac{A_H R}{12\pi\gamma_{wa}}\right)^{1/3}, \qquad [4]$$

which is approximately $H_c \approx 100$ nm for $A_H \sim 10^{-18}$ J (56), $R \sim 1$ mm, and $\gamma_{wa} = \gamma_{wo} + \gamma_{oa} \approx 65$ N/m.

For an oil film of thickness $H(r,t)$ and constant radius a, it can be assumed that $H \ll a$. Therefore, the lubrication approximation can be invoked, where only the radial velocity of the draining oil film, u_r, is considered. Neglecting inertial terms and assuming axisymmetry and an immobile interface (i.e., no plug flow), the Navier–Stokes velocity profile for a given film thickness is given by

$$u_r = \frac{\Delta P}{2\mu_o a}\left(z^2 - \left(\frac{H}{2}\right)^2\right), \qquad [5]$$

where z is the perpendicular distance from the center line of the oil film. Though it is likely that the film interfaces exhibit some degree of curvature and/or deformation (38, 42), an analytical approximation of the drainage rate may be obtained by assuming

rigid, parallel interfaces, such that $H(r,t) \rightarrow H(t)$ (full derivation in *SI Appendix*):

$$\frac{dH}{dt} = -\frac{1}{3\mu_o a^2}\left(\frac{\gamma_{wa} H^3(t)}{R} + \frac{A_H}{12\pi}\right). \quad [6]$$

Eq. **6** reveals that, all other parameters being equal, the drainage rate is inversely proportional to a^2, which is important because for conventional film drainage between two submerged same-sized water droplets of radius R, the point contact made between colliding droplets results in film drainage where $H \ll a \ll R$ (42); this is in sharp contrast to our large-area oil film that forms between two colliding droplets on an oil-infused surface, where $H \ll a \sim R$ (Fig. 2*A*, *Inset*). The large increase in the size of a is one possible explanation for the dramatically long lifetime of noncoalescence observed here compared with lifetimes reported for submerged droplets. Another possible reason is that droplets on an oil-infused surface require no external forces to collide together, whereas submerged droplets require gravity or an applied flow field which can accelerate the drainage rate.

By inserting electrodes into each of the noncoalescing droplets and applying a triangular waveform voltage, the average thickness of an oil film can be estimated:

$$H_{avg}(t) = \frac{\epsilon_r \epsilon_0 A}{C(t)}, \quad [7]$$

where ϵ_r is the relative permittivity of the oil (2.14 for hexadecane and 2.75 for silicone oils), $\epsilon_0 = 8.854 \times 10^{-12}$F/m is the vacuum permittivity, $A \approx 3 \times 10^{-6}$m^2 is the approximate surface area of the oil film between 5-μL droplets ($R \approx 1$ mm), and $C(t)$ is the capacitance calculated from current measurements (*SI Appendix*, Figs. S6 and S7). The electrodes were inserted into two separate 5-μL water droplets, and then the droplets were joined together using a micromanipulator to measure $H_{avg}(t)$ for the complete lifetime of noncoalescence (Fig. 3). For the remainder of the experiments shown here, a nonconductive superhydrophobic surface composed of silica nanoparticles on a glass slide (*SI Appendix*, Fig. S8) was used to prevent current from passing into the substrate.

For each trial, the oil film collapsed and coalescence occurred at a critical film thickness of $H_{avg}(t_c) \sim 0.1$–1 μm, ~1 order of magnitude larger than $H_c \approx 100$ nm predicted by Eq. **4**. It is therefore likely that the oil film exhibits a slight curvature in its profile, such that H_c is only obtained at a localized area with larger thicknesses elsewhere. Nevertheless, the parallel disk drainage model given by Eq. **6** reasonably approximated the experimental drainage rates (Fig. 3). Values of a used to fit Eq. **6** with the data ranged from $a \approx 100$ μm to $a \approx 850$ μm (depending on oil viscosity and excess oil thickness; *SI Appendix*, Table S3), which further supports the hypothesis that $a \sim R$ for air-stable interdroplet films. Though the insertion of electrodes into the droplets did reduce the lifetime of noncoalescence compared with free droplets (Fig. 2*A*), it was confirmed that the applied voltage did not have any appreciable effect on the capacitance measurements (*SI Appendix*, Fig. S9).

Air-Stable Droplet Interface Bilayers. Thus far, we have characterized the formation and drainage of a thin oil film between noncoalescing water droplets on an oil-infused surface. The functionality of these noncoalescing droplets would be greatly enhanced if the intermediate oil film could be replaced by a lipid bilayer, because a lipid membrane would provide a stable droplet–droplet interface of known thickness that can facilitate molecular transport between droplets. In this final section, we mixed 2.4 mM of diphytanoyl phosphocholine (DPhPC) phospholipids in the water phase before droplet deposition on the oil-infused surface. Colliding droplets still exhibit

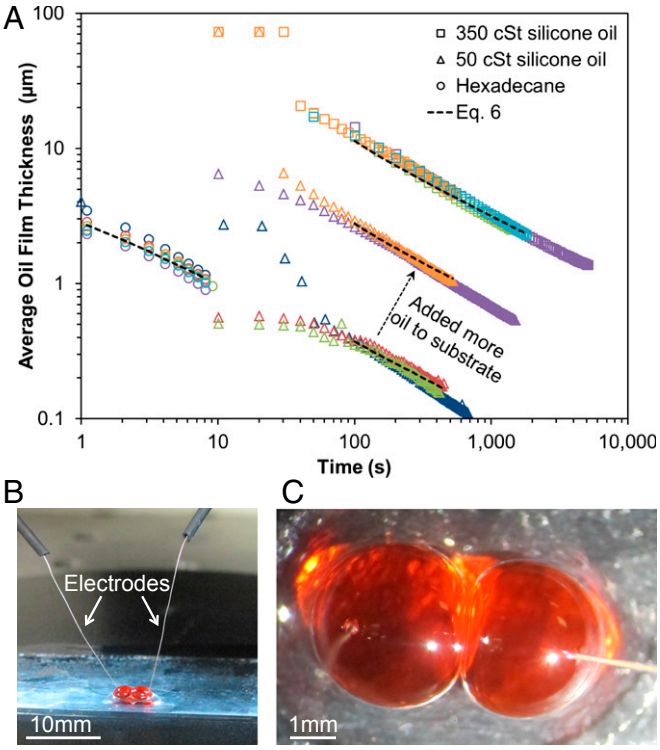

Fig. 3. (*A*) Electrical measurements of the average oil film thickness between noncoalescing water droplets for substrates infused with hexadecane (○) at room temperature (22 °C), 50 cSt silicone oil (△) cooled to the dew point (17 °C), or 350 cSt silicone oil (□) cooled to the dew point (now 7 °C due to change in humidity). Multiple trials for each oil are denoted by different colors, and the final data point for each trial indicates film collapse and coalescence. The drainage rates were in good agreement with the model (Eq. **6**) as denoted by the dotted trend lines; see *SI Appendix*, Table S3 for the values used in Eq. **6**. The initial film thickness increased with viscosity and could also be increased by adding more excess oil to the substrate, as demonstrated here with 50 cSt silicone oil. (*B* and *C*) Side-view and top-down photographs of noncoalescing water droplets with inserted electrodes.

noncoalescence in the same manner as before, but now lipids assemble at the interfaces of the intermediate oil film. Instead of droplet coalescence occurring once the oil film drains and collapses, the droplet–droplet interface is stabilized by the formation of a lipid bilayer that is only 5–7 nm thick (analogous to the formation of a black lipid membrane). Hexadecane oil was chosen for these experiments due to its compatibility with phospholipids and because its low viscosity ensures that the initial oil film will rapidly drain and become replaced by a droplet interface bilayer.

Using the same electrical characterization technique described in the previous section, capacitance measurements reveal that the oil film is completely replaced by a lipid bilayer within 50 s (Fig. 4*A*). Due to the high freezing temperature of hexadecane (18 °C), the surface could not be cooled down to the dew point, so over time the area of the bilayer steadily decreased to zero due to droplet evaporation. It is remarkable that the droplets never coalesced throughout the shrinkage of the droplet interface bilayer. In the future, a different choice of oil and/or humidity control could allow for the droplets to be held at the dew point; it should also be possible to use condensation in addition to evaporation to enable bilayers with reversibly tunable geometries.

Finally, we incorporated transmembrane peptides into the droplets to alter the ionic conductance of the interface as a way to verify that the lipid-stabilized interface between droplets is a bilayer membrane. Specifically, alamethicin peptides from the

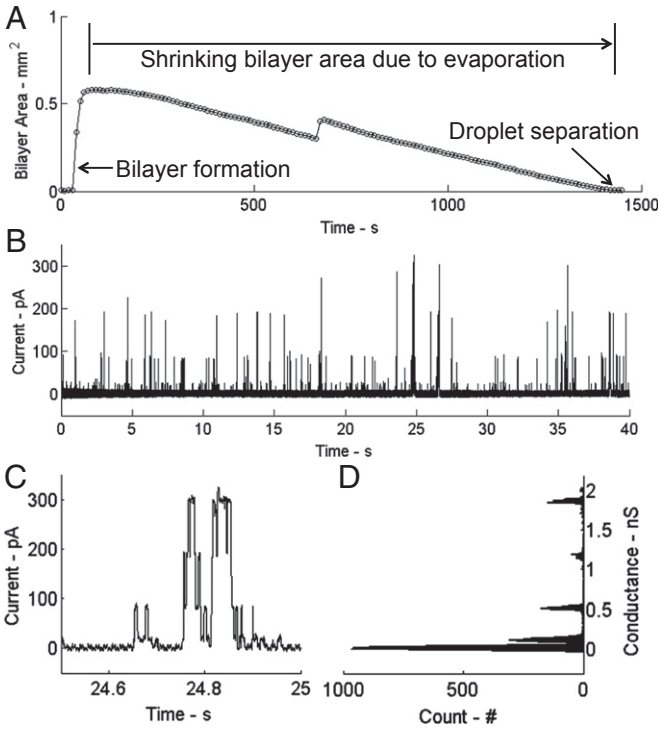

Fig. 4. (*A*) Bilayer area vs. time for an air-stable droplet interface bilayer. The area is determined from a capacitance measurement of the interface (*SI Appendix*). The maximum area (0.58 mm^2) corresponds to the maximum expansion of the thinned interface between droplets soon after initial bilayer formation, and the area reduces to zero over the next 23 min due to evaporation of the electrode-pinned droplets that causes them to pull apart as they shrink. The slight kink at $t \approx 700$ s was caused by one droplet suddenly shifting its position on the slippery surface. (*B*) Measurement of single-channel currents produced by alamethicin peptides at a voltage of +160 mV. (*C*) A detailed view of one gating event shows the characteristic, multilevel current response seen for alamethicin oligomers. (*D*) A corresponding histogram of the conductance levels.

fungus *Trichoderma viride* were incorporated into the droplets at 10 nM to encourage the formation of voltage-dependent ion channels through the bilayer. Fig. 4*B* shows measured current for a holding potential of +160 mV, where the transient increases correspond to the insertion and assembly of channel-forming alamethicin oligomers that span the thickness of the membrane. An example of the discrete changes in current that occur during these rapid pore-forming events is shown in more detail in Fig. 4*C*. A histogram of the channel conductance (i.e., current/voltage) during these gating transitions confirms the measured current levels to be those corresponding to the first four conductance levels (110 pS, 520 pS, 1.20 nS, and 1.85 nS) for alamethicin (59, 60). These results verify that the droplet–droplet interface is a bilayer membrane whose properties can be controlled and characterized using transmembrane biomolecules.

To our knowledge, this is the first report of fabricating a suspended lipid bilayer in an ambient environment. Black lipid membranes have always been confined to aqueous baths (45), and droplet interface bilayers have always been constructed in oil reservoirs (25) or in oil-in-water emulsions (61). Recent reports have obtained air-stable supported lipid membranes formed on a solid substrate (62, 63); however, the fluidity of such membranes is highly dependent on humidity, and transmembrane studies cannot be achieved with solid supported bilayers. Our air-stable droplet interface bilayers mitigate both of these limitations: the adjacent droplets maintain bilayer fluidity and suspend the bilayer to allow for molecular transport. The use of an oil-infused surface in place of an oil reservoir will enable the robust fabrication and modulation of functional droplet networks via techniques such as micropositioning, condensation, evaporation, vibration (64), or magnetic fields (65); such techniques are typically more practical in an ambient environment.

Conclusion

Using oil-infused superhydrophobic surfaces, we have demonstrated that colliding water droplets exhibit noncoalescence due to the spontaneous formation of a microscopic oil film between the droplets. In the absence of surfactants the Laplace pressure and intermolecular forces eventually cause the intermediate film to collapse, but the lifetime of noncoalescence is 1–3 orders of magnitude longer compared with droplets colliding in a submerged fluid bath. When phospholipids are mixed into the noncoalescing water droplets, an air-stable droplet interface bilayer forms that was used to detect single-channel gating events. To our knowledge, this is the first time that suspended lipid bilayers have been produced and characterized in an ambient environment instead of in a fluid reservoir. We envision that our air-stable suspended bilayers will enable the robust construction and manipulation of functional droplet networks and potentially allow for the stochastic biosensing of airborne molecules.

Materials and Methods

Superhydrophobic Silicon Nanopillars. The silicon nanopillars were fabricated using a lithography-free technique adapted from a previous report (66). First, 100 nm of silicon dioxide (SiO_2) was thermally grown onto a ⟨100⟩ Si substrate and 5 nm of platinum was then deposited onto the SiO_2 using an electron beam evaporator. The sample was heated in a rapid thermal processor furnace (Easy Tube 3000; First Nano) at full power for 8 s in a H_2 and Ar ambient to dewet the platinum film into an etch mask. The maximum temperature of the chamber at full power was ~850 °C. The SiO_2 was etched using 2 standard cubic centimeters per minute (sccm) O_2 and 45 sccm C_4F_8 for 55 s at 15 °C, 7 mTorr, and 200 W rf (Oxford Plasmalab 100). The Si was subsequently etched using 5 sccm Ar, 25 sccm SF_6, and 58 sccm C_4F_8 for 6 min at 20 °C, 10 mTorr, and 30 W RF. Scanning electron microscopy revealed an etch depth of 500 ± 100 nm and pillar diameters ranging from 10 to 100 nm (Fig. 1*E*). The nanostructure was rendered superhydrophobic by immersion in a solution of 0.1% (vol/vol) of (tridecafluoro-1,1,2,2-tetrahydrooctyl)triethoxysilane (Gelest Inc.) in hexane for 12 h. Droplets exhibited contact angles of $\theta_A = 168 \pm 3°$ and $\theta_R = 166 \pm 3°$ (66).

Superhydrophobic Glass. SiO_2 powder (*SI Appendix*, Fig. S8*A*) was annealed at 70 °C for 24 h. The mean size of the particle agglomerates was 610 ± 140 nm (*SI Appendix*, Fig. S8*B*). The powder was suspended in a solution of hexane and (tridecafluoro-1,1,2,2-tetrahydrooctyl)trichlorosilane (Gelest Inc.). The concentrations of the SiO_2 particles and silane in the hexane are 6 and 0.6 wt%, respectively. After stirring the suspension for 8 h at room temperature, the powder was washed with hexane to remove nonreacted silane groups and then dried at 60 °C for 24 h. The resulting functionalized particles (*SI Appendix*, Fig. S8*C*) were suspended in a solution of polyurethane resin and acetone in a weight ratio $W_{particle} : W_{resin} : W_{acetone} = 1 : 1 : 20$. Superhydrophobic substrates with water contact angle ~170° were obtained by spin coating the suspension with a Speedline Technologies G3-8 at 1,000 rpm for 30 s on glass slides (*SI Appendix*, Fig. S8*D*).

Electrical Measurements. Electrical measurements of oil- and bilayer-stabilized interfaces were performed by measuring the current induced by a triangle waveform voltage applied to two wire-type silver–silver chloride electrodes (125 μm) inserted into the droplets. The triangle voltage waveform was the output of a function generator (Agilent 33210A), and the resulting current was recorded using an Axopatch 200B patch-clamp amplifier and Digidata 1440A data acquisition device (Molecular Devices). Measurements of current were sampled at 20 kHz, and all electrical measurements are performed on glass substrates.

Droplets Solutions for Bilayer Tests. Hexadecane [99% (vol/vol); Sigma] was used as the infusing oil on the glass substrates for bilayer formation between droplets. Liposome solutions consisted of 2.4 mM DPhPC (Avanti Polar Lipids) suspended as 100-nM liposomes in a 200-mM NaCl (Sigma), 10-mM Mops (Sigma) buffer. Alamethicin peptides (A.G. Scientific) were stored in ethanol at 10 mg/mL, and then diluted to 10 nM (19.64 ng/mL) in liposome solution.

ACKNOWLEDGMENTS. We thank J. Fowlkes, P. Rack, and S. Retterer for helpful discussions. This research was conducted at the Center for Nanophase Materials Sciences, which is sponsored at Oak Ridge National Laboratory by the Scientific User Facilities Division, Office of Basic Energy Sciences, US Department of Energy. Funding was provided by Air Force Office of Scientific Research Basic Research Initiative Grant FA9550-12-1-0464 (to S.A.S.) and the SunShot Program of the Office of Energy Efficiency and Renewable Energy (G.P.).

1. Bohn HF, Federle W (2004) Insect aquaplaning: Nepenthes pitcher plants capture prey with the peristome, a fully wettable water-lubricated anisotropic surface. *Proc Natl Acad Sci USA* 101(39):14138–14143.
2. Verheijen HJJ, Prins MWJ (1999) Reversible electrowetting and trapping of charge: model and experiments. *Langmuir* 15(20):6616–6620.
3. Krupenkin T, Yang S, Mach P (2003) Tunable liquid microlens. *Appl Phys Lett* 82: 316–318.
4. Quere D (2005) Non-sticking drops. *Rep Prog Phys* 68(11):2495–2532.
5. Wong TS, et al. (2011) Bioinspired self-repairing slippery surfaces with pressure-stable omniphobicity. *Nature* 477(7365):443–447.
6. Tuteja A, et al. (2007) Designing superoleophobic surfaces. *Science* 318(5856): 1618–1622.
7. Daniel D, Mankin MN, Belisle RA, Wong TS, Aizenberg J (2013) Lubricant-infused micro/nano-structured surfaces with tunable dynamic omniphobicity at high temperatures. *Appl Phys Lett* 102:231603.
8. Yao X, et al. (2013) Adaptive fluid-infused porous films with tunable transparency and wettability. *Nat Mater* 12(6):529–534.
9. Anand S, Paxson AT, Dhiman R, Smith JD, Varanasi KK (2012) Enhanced condensation on lubricant-impregnated nanotextured surfaces. *ACS Nano* 6(11):10122–10129.
10. Xiao R, Miljkovic N, Enright R, Wang EN (2013) Immersion condensation on oil-infused heterogeneous surfaces for enhanced heat transfer. *Sci Rep* 3:1988.
11. Liu H, Zhang P, Liu M, Wang S, Jiang L (2013) Organogel-based thin films for self-cleaning on various surfaces. *Adv Mater* 25(32):4477–4481.
12. Lalia BS, Anand S, Varanasi KK, Hashaikeh R (2013) Fog-harvesting potential of lubricant-impregnated electrospun nanomats. *Langmuir* 29(42):13081–13088.
13. Shillingford C, MacCallum N, Wong TS, Kim P, Aizenberg J (2014) Fabrics coated with lubricated nanostructures display robust omniphobicity. *Nanotechnology* 25(1): 014019.
14. Kim P, et al. (2012) Liquid-infused nanostructured surfaces with extreme anti-ice and anti-frost performance. *ACS Nano* 6(8):6569–6577.
15. Wilson PW, et al. (2013) Inhibition of ice nucleation by slippery liquid-infused porous surfaces (SLIPS). *Phys Chem Chem Phys* 15(2):581–585.
16. Zhu L, et al. (2013) Ice-phobic coatings based on silicon-oil-infused polydimethylsiloxane. *ACS Appl Mater Interfaces* 5(10):4053–4062.
17. Subramanyam SB, Rykaczewski K, Varanasi KK (2013) Ice adhesion on lubricant-impregnated textured surfaces. *Langmuir* 29(44):13414–13418.
18. Epstein AK, Wong TS, Belisle RA, Boggs EM, Aizenberg J (2012) Liquid-infused structured surfaces with exceptional anti-biofouling performance. *Proc Natl Acad Sci USA* 109(33):13182–13187.
19. Lafuma A, Quere D (2011) Slippery pre-suffused surfaces. *Europhys Lett* 96:56001.
20. Hejazi V, Nosonovsky M (2012) Wetting transitions in two-, three-, and four-phase systems. *Langmuir* 28(4):2173–2180.
21. Smith JD, et al. (2013) Droplet mobility on lubricant-impregnated surfaces. *Soft Matter* 9:1772–1780.
22. Jenner E, D'Urso B (2013) Wetting states on structured immiscible liquid coated surfaces. *Appl Phys Lett* 103:251606.
23. McLean JD, Kilpatrick PK (1997) Effects of asphaltene solvency on stability of water-in-crude-oil emulsions. *J Colloid Interface Sci* 189:242–253.
24. Funakoshi K, Suzuki H, Takeuchi S (2006) Lipid bilayer formation by contacting monolayers in a microfluidic device for membrane protein analysis. *Anal Chem* 78(24): 8169–8174.
25. Leptihn S, et al. (2013) Constructing droplet interface bilayers from the contact of aqueous droplets in oil. *Nat Protoc* 8(6):1048–1057.
26. Holden MA, Needham D, Bayley H (2007) Functional bionetworks from nanoliter water droplets. *J Am Chem Soc* 129(27):8650–8655.
27. Sarles SA, Leo DJ (2010) Physical encapsulation of droplet interface bilayers for durable, portable biomolecular networks. *Lab Chip* 10(6):710–717.
28. Sarles SA, Leo DJ (2010) Regulated attachment method for reconstituting lipid bilayers of prescribed size within flexible substrates. *Anal Chem* 82(3):959–966.
29. Punnamaraju S, Steckl AJ (2011) Voltage control of droplet interface bilayer lipid membrane dimensions. *Langmuir* 27(2):618–626.
30. Dixit SS, Pincus A, Guo B, Faris GW (2012) Droplet shape analysis and permeability studies in droplet lipid bilayers. *Langmuir* 28(19):7442–7451.
31. Boreyko JB, Mruetusatorn P, Sarles SA, Retterer ST, Collier CP (2013) Evaporation-induced buckling and fission of microscale droplet interface bilayers. *J Am Chem Soc* 135(15):5545–5548.
32. Hwang WL, Holden MA, White S, Bayley H (2007) Electrical behavior of droplet interface bilayer networks: Experimental analysis and modeling. *J Am Chem Soc* 129(38):11854–11864.
33. Aghdaei S, Sandison ME, Zagnoni M, Green NG, Morgan H (2008) Formation of artificial lipid bilayers using droplet dielectrophoresis. *Lab Chip* 8(10):1617–1620.
34. Zagnoni M, Sandison ME, Marius P, Morgan H (2009) Bilayer lipid membranes from falling droplets. *Anal Bioanal Chem* 393(6-7):1601–1605.
35. Sarles SA (2013) The use of virtual ground to control transmembrane voltages and measure bilayer currents in serial arrays of droplet interface bilayers. *Smart Mater Struct* 22(9):094023.
36. Hwang WL, Chen M, Cronin B, Holden MA, Bayley H (2008) Asymmetric droplet interface bilayers. *J Am Chem Soc* 130(18):5878–5879.
37. Marrucci G (1969) A theory of coalescence. *Chem Eng Sci* 24:975–985.
38. Chesters AK (1991) The modelling of coalescence processes in fluid-liquid dispersions: A review of current understanding. *Chem Eng Res Des* 69:259–270.
39. Yiantsios SG, Davis RH (1991) Close approach and deformation of two viscous drops due to gravity and van der Waals forces. *J Colloid Interface Sci* 144:412–433.
40. Steinhaus B, Spicer PT, Shen AQ (2006) Droplet size effects on film drainage between droplet and substrate. *Langmuir* 22(12):5308–5313.
41. Abid S, Chesters AK (1994) The drainage and rupture of partially-mobile films between colliding drops at constant approach velocity. *Int J Multiph Flow* 20:613–629.
42. Klaseboer E, Chevaillier JP, Gourdon C, Masbernat O (2000) Film drainage between colliding drops at constant approach velocity: Experiments and modeling. *J Colloid Interface Sci* 229:274–285.
43. Borrell M, Leal LG (2008) Viscous coalescence of expanding low-viscosity drops; the dueling drops experiment. *J Colloid Interface Sci* 319:263–269.
44. Wang W, Gong J, Ngan KH, Angeli P (2009) Effect of glycerol on the binary coalescence of water drops in stagnant oil phase. *Chem Eng Res Des* 87:1640–1648.
45. Montal M, Mueller P (1972) Formation of bimolecular membranes from lipid monolayers and a study of their electrical properties. *Proc Natl Acad Sci USA* 69(12): 3561–3566.
46. Kasianowicz JJ, Brandin E, Branton D, Deamer DW (1996) Characterization of individual polynucleotide molecules using a membrane channel. *Proc Natl Acad Sci USA* 93(24):13770–13773.
47. Howorka S, Cheley S, Bayley H (2001) Sequence-specific detection of individual DNA strands using engineered nanopores. *Nat Biotechnol* 19(7):636–639.
48. Bayley H, Cremer PS (2001) Stochastic sensors inspired by biology. *Nature* 413(6852): 226–230.
49. Guan X, Gu LQ, Cheley S, Braha O, Bayley H (2005) Stochastic sensing of TNT with a genetically engineered pore. *ChemBioChem* 6(10):1875–1881.
50. Poulos JL, et al. (2009) Ion channel and toxin measurement using a high throughput lipid membrane platform. *Biosens Bioelectron* 24(6):1806–1810.
51. Sapra KT, Bayley H (2012) Lipid-coated hydrogel shapes as components of electrical circuits and mechanical devices. *Sci Rep* 2:848.
52. Maglia G, et al. (2009) Droplet networks with incorporated protein diodes show collective properties. *Nat Nanotechnol* 4(7):437–440.
53. Villar G, Graham AD, Bayley H (2013) A tissue-like printed material. *Science* 340(6128): 48–52.
54. Vogel N, Belisle RA, Hatton B, Wong TS, Aizenberg J (2013) Transparency and damage tolerance of patternable omniphobic lubricated surfaces based on inverse colloidal monolayers. *Nat Commun* 4:3167.
55. Kim P, Kreder MJ, Alvarenga J, Aizenberg J (2013) Hierarchical or not? Effect of the length scale and hierarchy of the surface roughness on omniphobicity of lubricant-infused substrates. *Nano Lett* 13(4):1793–1799.
56. Carlson A, Kim P, Amberg G, Stone HA (2013) Short and long time drop dynamics on lubricated substrates. *Europhys Lett* 104:34008.
57. Eggers J, Lister JR, Stone HA (2013) Coalescence of liquid drops. *J Fluid Mech* 401: 293–310.
58. Steyer A, Guenoun P, Beysens D, Knobler CM (1990) Two-dimensional ordering during droplet growth on a liquid surface. *Phys Rev B Condens Matter* 42(1):1086–1089.
59. Sansom MSP (1991) The biophysics of peptide models of ion channels. *Prog Biophys Mol Biol* 55(3):139–235.
60. Sarles SA, Stiltner LJ, Williams CB, Leo DJ (2010) Bilayer formation between lipid-encased hydrogels contained in solid substrates. *ACS Appl Mater Interfaces* 2(12): 3654–3663.
61. Villar G, Heron AJ, Bayley H (2011) Formation of droplet networks that function in aqueous environments. *Nat Nanotechnol* 6(12):803–808.
62. Holden MA, Jung SY, Yang T, Castellana ET, Cremer PS (2004) Creating fluid and air-stable solid supported lipid bilayers. *J Am Chem Soc* 126(21):6512–6513.
63. Albertorio F, et al. (2005) Fluid and air-stable lipopolymer membranes for biosensor applications. *Langmuir* 21(16):7476–7482.
64. Noblin X, Kofman R, Celestini F (2009) Ratchetlike motion of a shaken drop. *Phys Rev Lett* 102(19):194504.
65. Timonen JVI, Latikka M, Leibler L, Ras RHA, Ikkala O (2013) Switchable static and dynamic self-assembly of magnetic droplets on superhydrophobic surfaces. *Science* 341(6143):253–257.
66. Boreyko JB, et al. (2013) Dynamic defrosting on nanostructured superhydrophobic surfaces. *Langmuir* 29(30):9516–9524.

Supporting Information Appendix

Air-stable droplet interface bilayers on oil-infused surfaces

Jonathan B. Boreyko[1], Georgios Polizos[2], Panos G. Datskos[2], Stephen A. Sarles*[,3], and C. Patrick Collier*[,1]

[1]Center for Nanophase Materials Sciences, Oak Ridge National Laboratory, Oak Ridge, TN 37831
[2]Energy and Transportation Science Division, Oak Ridge National Laboratory, Oak Ridge, TN 37831
[3]Department of Mechanical, Aerospace, and Biomedical Engineering, The University of Tennessee, Knoxville, TN 37996

*Address correspondence to colliercp@ornl.gov; ssarles@utk.edu

Derivation of film drainage rate:

Assumptions regarding thin-film drainage between two droplets:

- The two droplets are same-sized ($R_1 = R_2 = R$)
- Film interfaces are rigid and parallel, such that the film thickness $H(t)$ does not vary along the radial axis when using cylindrical coordinates
- Film radius (a) is constant over time
- Neglect inertial terms (viscous dominated flow)
- Lubrication approximation (only solve for radial drainage velocity, $u_r(z,t)$)
- Laminar (Poiseuille-type) flow, such that $\frac{\partial P}{\partial r} = -\frac{\Delta P(t)}{a}$

Combining all of these assumptions results in the following Navier-Stokes equation:

$$\frac{\Delta P(t)}{a} = \mu_o \frac{\partial^2 u_r(z,t)}{\partial z^2}, \text{ BCs: } u_r\left(\frac{H}{2}, t\right) = u_r\left(-\frac{H}{2}, t\right) = 0. \quad \text{(S1)}$$

Which yields the solution:

$$u_r(z,t) = \frac{\Delta P(t)}{2a\mu_o}\left(z^2 - \left(\frac{H(t)}{2}\right)^2\right). \quad \text{(S2)}$$

The volumetric flow rate of oil draining about the outer radius of the film is given by:

$$Q(t) = 2\pi a \int_{-H/2}^{H/2} u_r(z,t)dz, \quad \text{(S3)}$$

$$Q(t) = -\frac{\pi \Delta P(t)}{6\mu_o} H^3(t). \quad \text{(S4)}$$

Finally, Eq. S4 can be linked to the change in film thickness over time:

$$\frac{dH}{dt} = \frac{Q(t)}{\pi a^2}. \quad \text{(S5)}$$

Using the expression for ΔP defined by Eq. 3 in the manuscript results in:

$$\frac{dH}{dt} = -\frac{1}{3\mu_o a^2}\left(\frac{\gamma_{wa} H^3(t)}{R} + \frac{A_H}{12\pi}\right) \quad \text{(S6)}$$

Eq. S6, which is identical to Eq. 6 in the manuscript, was solved numerically to plot the theoretical values of $H(t)$ over the experimental data in Figure 3. All variables were held constant (see Table S3) and the value for the film radius a was adjusted to best fit the theoretical data with the averaged values of the experimental trials for each oil.

Capacitance measurements for estimating film thickness:

This study utilized electrical measurements to estimate the thickness of the draining oil film between droplets. Because the oil is a dielectric, the fluid interface behaves like a capacitor, whose capacitance is proportional to the dielectric permittivity of the oil film and the area of contact between droplets and inversely proportional to the thickness of the film. Therefore to estimate thickness, we first measure the capacitance of the interface. The capacitance is determined indirectly by measuring the current induced by a triangle waveform voltage applied across the interface.

For the experiments depicted in Figs. 3 and 4, a triangular waveform voltage was applied between two 5 μL droplets and the resulting current was measured. The current was in the shape of a square waveform; as the oil drains, the current increases in amplitude but always remains a square wave in shape (Fig. S6).

For square current waveforms, capacitance is determined using

$$C = \frac{|i|}{dV/dt}, \tag{S7}$$

where, $|i|$ is the amplitude of the measured current and dV/dt is the time rate of change of the applied voltage. For a triangle waveform, dV/dt is equal to $4A_V f$, where A_V and f are the amplitude and frequency of the voltage, respectively. This calculation is performed using MATLAB® locally within each current versus time measurement to extract estimates of capacitance versus time for the interface (Fig. S7).

To characterize film drainage over time (Fig. 3), the average thickness of the oil interface is estimated from the capacitance values using:

$$H_{avg}(t) = \frac{\varepsilon_r \varepsilon_0 A}{C(t)}, \tag{S8}$$

where ε_r is the relative permittivity for the oil (ε_r = 2.14 for hexadecane, ε_r = 2.75 for silicone oils,), ε_0 is the permittivity of free space in vacuum (8.854 x 10^{-12} F/m), A is the area of the interface (assumed to be 3mm^2 for connected 5uL droplets), and $C(t)$ are the values of capacitance extracted from the current measurement.

When introducing lipids into the system, the draining oil film eventually gets replaced by a lipid bilayer (Fig. 4). In this case, the thickness of the interface is now constant ($H_b \approx 6 \pm 1$ nm for DPhPC) and the evolving area of the droplet interface bilayer can be extracted:

$$A(t) = \frac{C(t) H_b}{\varepsilon_r \varepsilon_0}. \tag{S9}$$

Table S1: Physical properties of oils used to infuse the superhydrophobic surfaces. Temperatures below room temperature correspond to the dew point temperatures used in the experiments to prevent evaporation. Viscosity and density values are from the manufacturers and are accurate to within 10%.

Oil Type	***T* (°C)**	**ν (cSt)**	**ρ (kg/m^3)**	**μ (mPa·s)**
Hexadecane	25	4	773	3
Krytox 100	8	25	1,854	46
	20	12.4	1,830	23
50 cSt Silicone Oil	8	75	975	73
	17	60	967	58
	25	50	960	48
350 cSt Silicone Oil	8	500	983	492
	25	350	968	339
Fomblin 25/6	8	517	1,900	982
	20	276	1,900	524

Table S2: Surface tension measurements at room temperature for the oils used to infuse the superhydrophobic surfaces. The values for hexadecane come from the literature,[1] all other values are measured using a goniometer (Fig. S1).

Oil Type	**γ_{oa} (mN/m)**	**γ_{ow} (mN/m)**
Hexadecane	27	55
Krytox 100	16	53
50 cSt Silicone Oil	21	41
350 cSt Silicone Oil	20	35
Fomblin 25/6	18	Non-constant

[1] Goebel A, Lunkenheimer K (1997) Interfacial tension of the water/n-alkane interface. Langmuir 13:369-372.

Table S3: Values plugged into Eq. 6 to estimate the theoretical drainage rate of the oil films. The surface tension and viscosity values are from Tables S1 and S2, the constant film radius a was chosen to best fit the model to the experimental results (Fig. 3), and R is the approximate size of the droplets used in the experiments. The initial thickness of the film, $H(t_i)$, was set to the earliest experimental value where all trials converged (at time t_i).

Oil Type	**γ_{wa} (mN/m)**	**μ (mPa·s)**	***a* (μm)**	***R* (mm)**	**A_H (J)**	**t_i (s)**	**$H(t_i)$ (μm)**
Hexadecane	72	3	400	1.0	10^{-18}	1	2.72
50 cSt Silicone Oil	62	58	95	1.0	10^{-18}	100	0.37
50 cSt Silicone Oil (more oil added)	62	58	650	1.0	10^{-18}	100	2.77
350 cSt Silicone Oil	55	492	850	1.0	10^{-18}	100	11.37

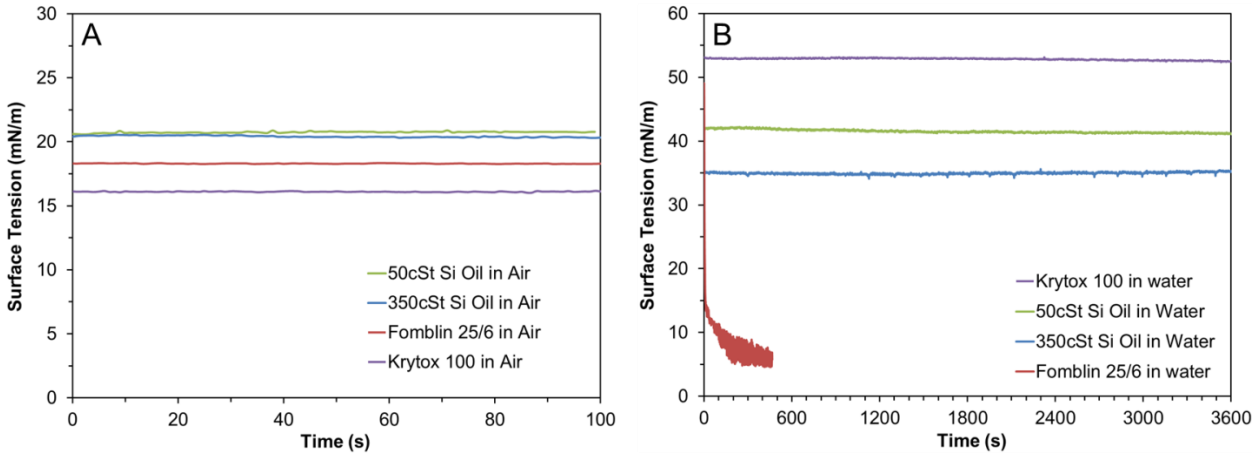

Fig. S1: Surface tension measurements for (A) oil-air and (B) oil-water interfaces using the pendant drop method with a goniometer (Rame-Hart Model 590). With the exception of the Fomblin 25/6 oil, the oil-water surface tension values remained constant over the course of an hour, confirming that they contain a negligible amount of surface-active material. The surfactant present in the Fomblin 25/6 oil served to stabilize the droplet-droplet interface, such that droplet coalescence did not occur even after 24 hours (see Fig. S5).

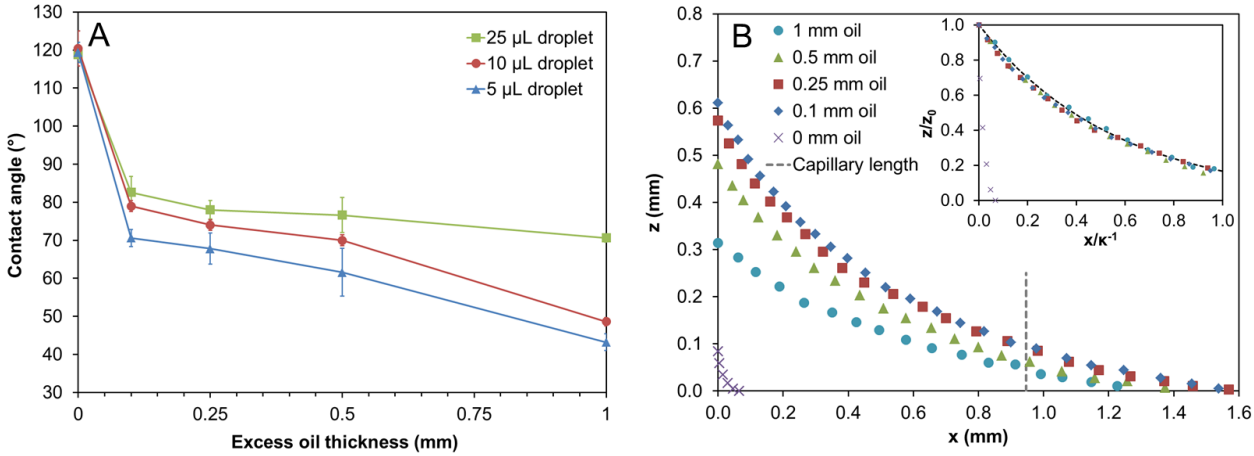

Fig. S2: (A) The contact angle of water droplets (at 21 °C) could be tuned by varying the amount of excess oil deposited onto the surface. Smaller droplets were more sensitive to changes in oil excess compared to larger droplets. Krytox 100 oil was used for all trials and was spin-coated at 1,000 RPM for 45 s for the data points corresponding to a negligible excess thickness. Five trials were taken for each data point and error bars represent a 95% confidence interval. (B) The profile of a Krytox oil meniscus extending from the contact line of a 5 µL water droplet exhibited an exponential decay that scaled to the capillary length: $\kappa^{-1} \sim \sqrt{\gamma/\rho g}$. Initially, the height of the oil meniscus grew with increasing excess oil; however, for oil layers exceeding 0.1 mm the meniscus actually became smaller with increasing oil excess. This is most likely due to the fact that the droplet's contact angle decreases with increasing oil excess, such that the oil interface does not need to rise as dramatically to find its equilibrium angle at the droplet's contact line. Inset: for non-limiting oil films, the profiles of all oil menisci collapsed onto a single curve when the x-coordinates were non-dimensionalized by the capillary length (x/κ^{-1}). The dotted line corresponds to the equation for exponential decay: $z(x) \approx z_0 e^{-\varphi \kappa x}$, where z_0 is the height of the meniscus at the contact line, $\varphi \approx 2$, and x is the horizontal distance from the contact line.

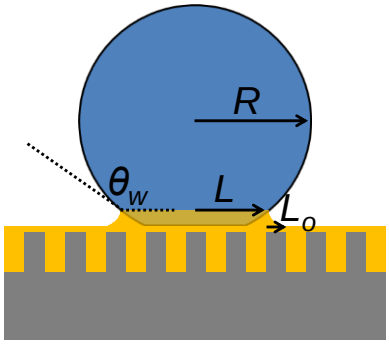

Fig. S3: Schematic of a water droplet on an oil-infused surface. Colliding droplets exhibit non-coalescence when $\theta_W < 90°$. When $\theta_W > 90°$, droplets will only exhibit non-coalescence when $R < L + L_O$ (see Eq. 1 in manuscript).

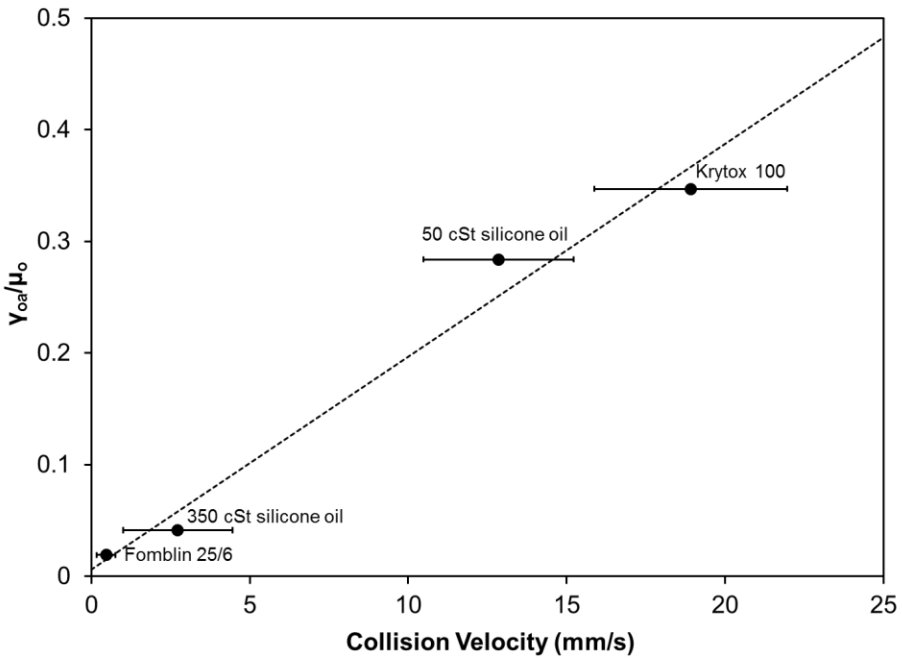

Fig. S4: The collision velocity of two adjacent water droplets was directly proportional to the viscous-capillary velocity of the oil: $v \approx 0.02(\gamma_{oa}/\mu_o)$ where v is in mm/s (dotted line). To obtain droplet collision, two 5 µL water droplets were placed on the oil-infused surface such that their oil menisci overlapped, causing them to join together by the surface tension of the oil. The collision velocity was measured using a side-view camera and was taken as the maximum cumulative velocity attained by the droplets before deceleration. To prevent evaporation, the surface was held at 8 °C. Ten trials were performed for the Krytox 100 and five trials were performed for the other oils. Uncertainty corresponds to a 95% confidence interval.

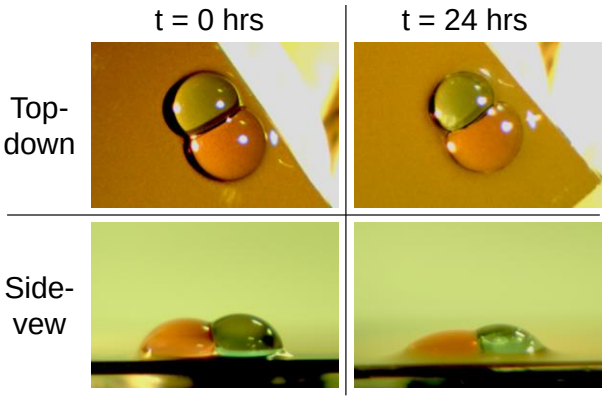

Fig. S5: Two water droplets on a surface infused with Fomblin 25/6 oil exhibited non-coalescence even after 24 hours. This is most likely due to the presence of surfactant in the Fomblin 25/6, which can stabilize the droplet-droplet interface during film drainage. Droplets were 10 µL and the surface was held at 8 °C to minimize evaporation. Red and green food coloring were added to the respective drops to illustrate the non-coalescence.

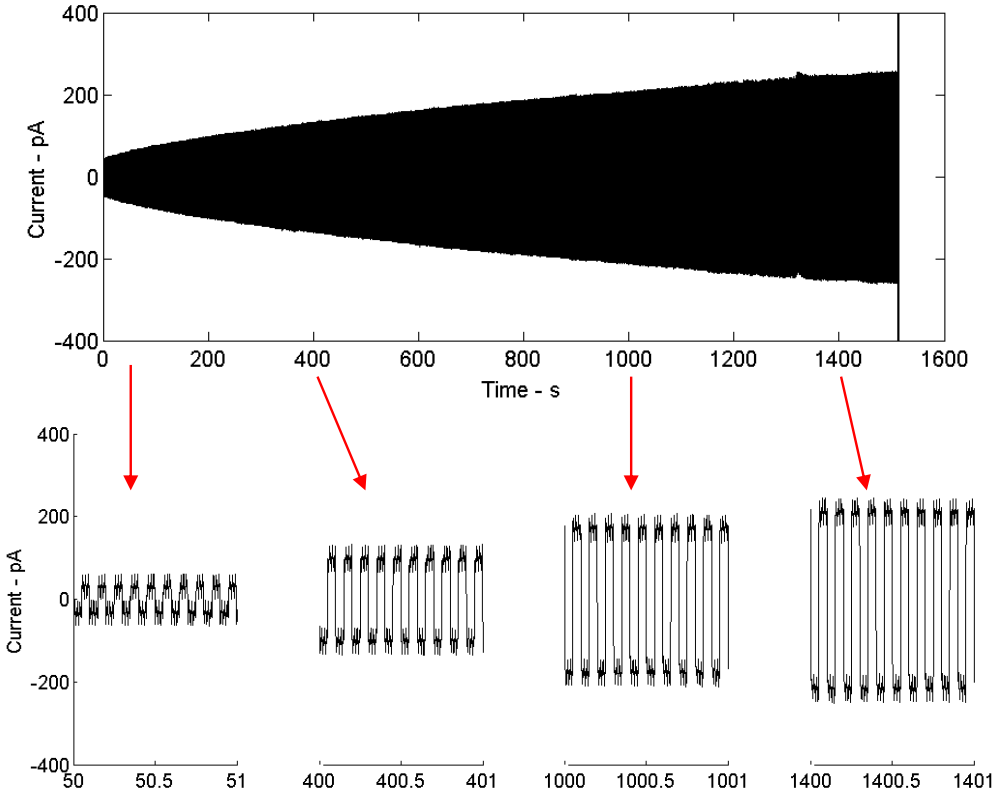

Fig. S6: The current produced by a 40mV, 10Hz triangle voltage during the draining of 50 cSt oil film from between two 5μL droplets. The raw current increases in amplitude during the 25-minute period as the oil film drains, and then abruptly increases when the oil film finally ruptures (t = 1512 s). Prior to rupture, the current remains a square wave, with only the amplitude increasing in time as the film thins.

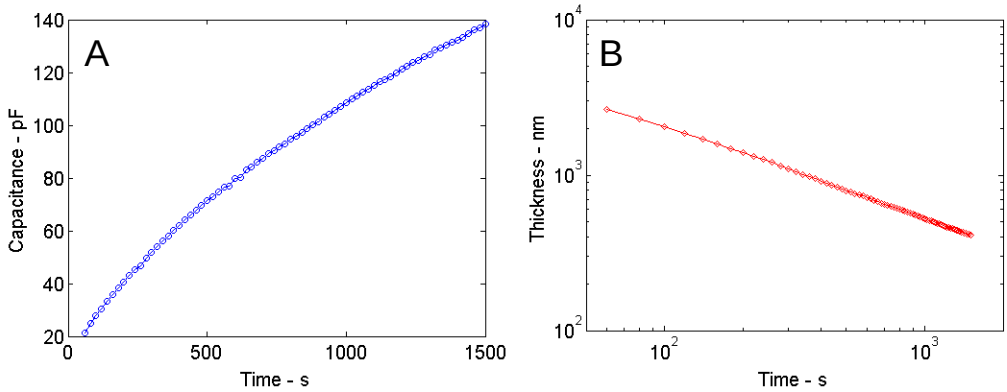

Fig. S7: Example of converting capacitance to film thickness. (A) The computed capacitance values increase nearly 7-fold during the 25 minutes it took the 50 cSt oil to drain before rupture. (B) During film drainage, the average thickness of the oil film decreased from ≈ 2 μm to ≈ 400 nm, at which point the film ruptures.

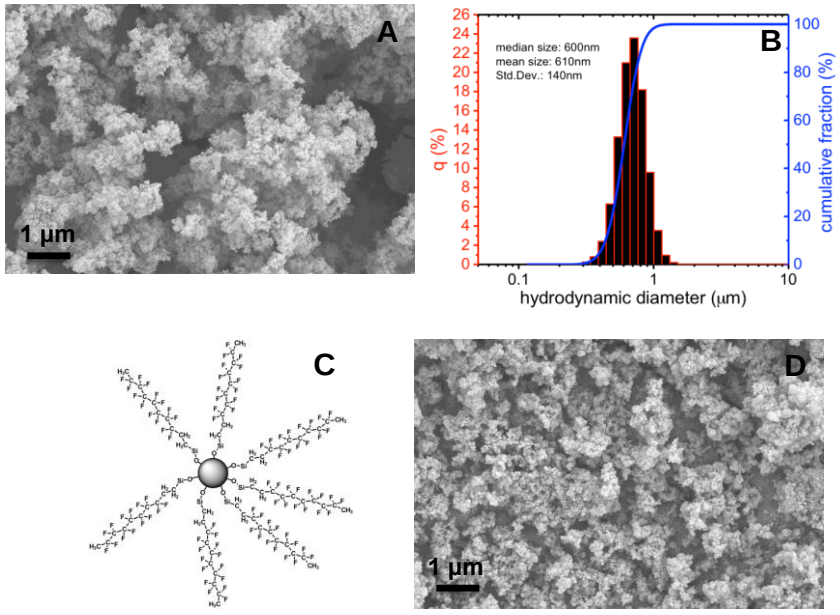

Fig. S8: (A) SEM image of the SiO_2 particle agglomerates prior to functionalization. (B) Particle size distribution of the as received SiO_2 powder according to laser diffraction patterns. The size of the agglomerates is indicated on the plot. For any diameter *x*, the cumulative fraction is the percentage of the particles whose diameter lies below *x*. (C) A schematic illustration of SiO_2 nanoparticles functionalized with fluorosilanes. (D) SEM image of a glass substrate coated with functionalized nanoparticles. The water contact angle is approximately 170°.

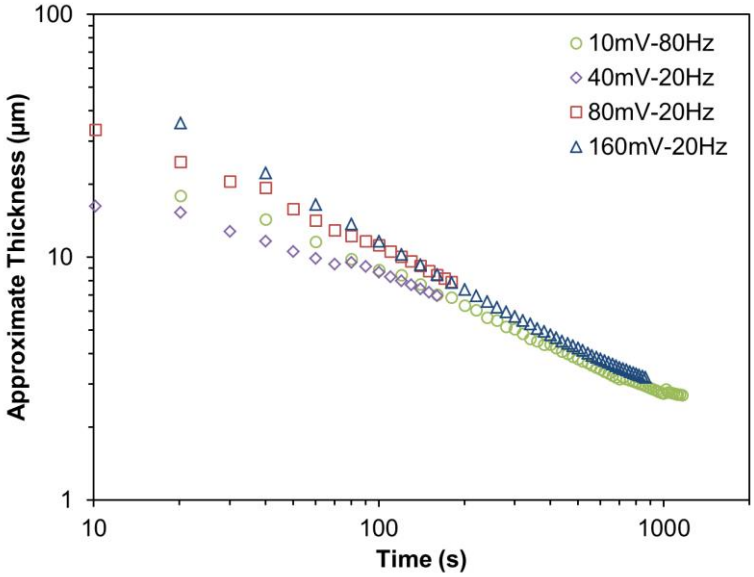

Fig. S9: To verify that the applied voltage does not directly affect the thickness of the oil film, four different voltages were applied to 5 µL droplets on a surface infused with 350 cSt silicone oil. The thickness measurements did not vary with changing amplitude or frequency of the applied voltage.

Movie S1: Side-view movie of coalescence between 5 μL water droplets on an oil-infused surface (see Fig. 1A). Krytox 100 was spin-coated onto the surface at 1,000 RPM for 45 s. Coalescence always occurred when the droplets first contacted at the water-air interfaces. The field of view is 6.8 mm × 5.1 mm and the movie is in real time.

Movie S2: Side-view movie of non-coalescence between 5 μL water droplets on an oil-infused surface (see Fig. 1B). Krytox 100 was spin-coated onto the surface at 500 RPM for 45 s. The non-coalescence occurs because of the overlapping oil menisci, which pull together to squeeze a thin film of oil between the droplets. The field of view is 6.8 mm × 5.1 mm and the movie is in real time.

Movie S3: Top-down imaging of a non-coalescing droplet network (see Fig. 1D). Each droplet is 10 μL and the network spontaneously evolves into close-packed hexagonal droplets to minimize surface energy. The field of view is 10 mm × 10 mm and the movie is played back at 30X fast-forward.

Movie S4: Side-view movie of lifetime of non-coalescence for two 5 μL water droplets on a surface infused with Krytox 100 oil (see Fig. 2B). The thin film between the droplets lasts for 196 s before rupture and coalescence occurs. The field of view is 6.8 mm × 5.1 mm and the movie is played back at 3X fast-forward.

Movie S5: Side-view movie of lifetime of non-coalescence for two 5 μL water droplets on a surface infused with 50 cSt oil (see Fig. 2C). The thin film between the droplets lasts for 1,261 s before rupture and coalescence occurs. The field of view is 6.8 mm × 5.1 mm and the movie is played back at 30X fast-forward.

Supporting Information

Boreyko et al. 10.1073/pnas.1400381111

Movie S1. Side-view movie of coalescence between 5-μL water droplets on an oil-infused surface (Fig. 1*A*). Krytox 100 was spin-coated onto the surface at 1,000 rpm for 45 s. Coalescence always occurred when the droplets first contacted at the water–air interfaces. The field of view is 6.8 × 5.1 mm, and the movie is in real time.

Movie S1

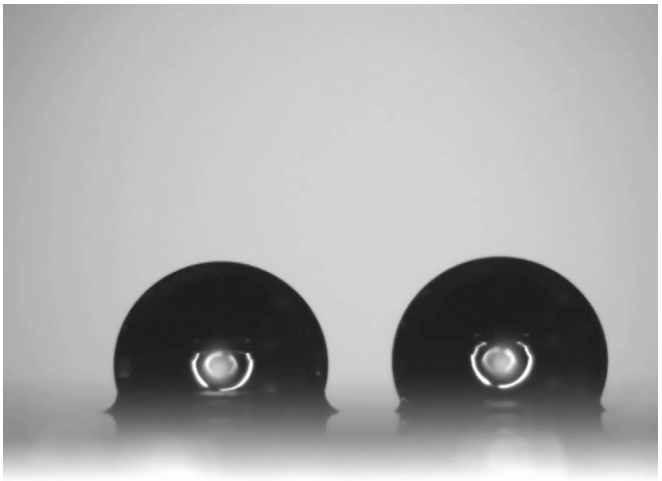

Movie S2. Side-view movie of noncoalescence between 5-μL water droplets on an oil-infused surface (Fig. 1*B*). Krytox 100 was spin-coated onto the surface at 500 rpm for 45 s. The noncoalescence occurs because of the overlapping oil menisci, which pull together to squeeze a thin film of oil between the droplets. The field of view is 6.8 × 5.1 mm, and the movie is in real time.

Movie S2

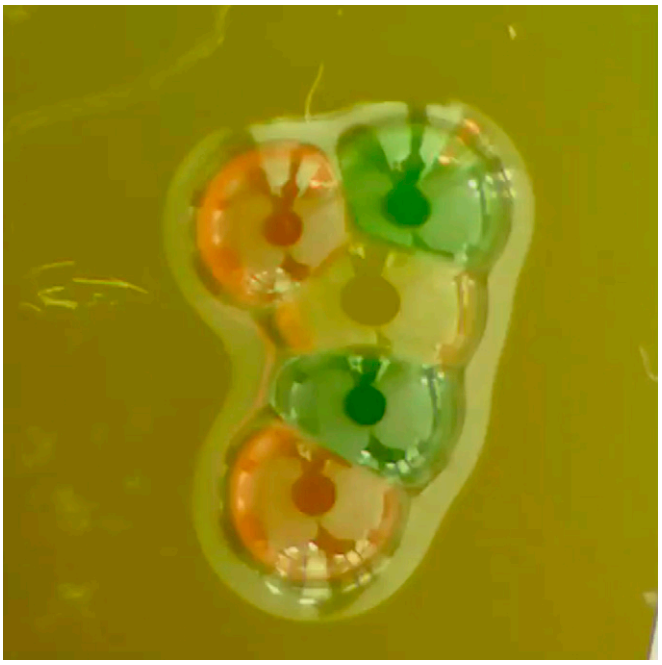

Movie S3. Top-down imaging of a noncoalescing droplet network (Fig. 1*D*). Each droplet is 10 μL, and the network spontaneously evolves into close-packed hexagonal droplets to minimize surface energy. The field of view is 10 × 10 mm, and the movie is played back at 30× fast-forward.

Movie S3

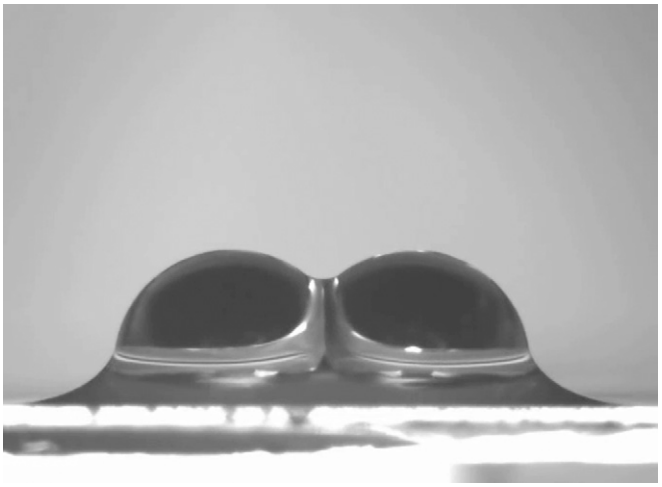

Movie S4. Side-view movie of lifetime of noncoalescence for two 5-μL water droplets on a surface infused with Krytox 100 oil (Fig. 2*B*). The thin film between the droplets lasts for 196 s before rupture and coalescence occurs. The field of view is 6.8 × 5.1 mm, and the movie is played back at 3× fast-forward.

Movie S4

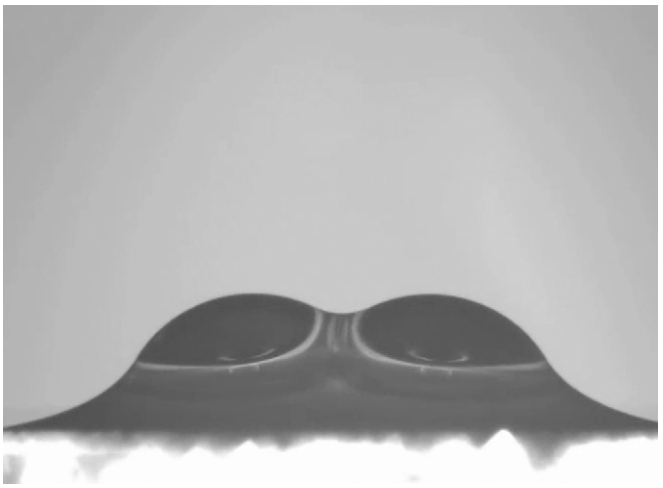

Movie S5. Side-view movie of lifetime of noncoalescence for two 5-μL water droplets on a surface infused with 50 cSt oil (*SI Appendix*, Fig. S2*C*). The thin film between the droplets lasts for 1,261 s before rupture and coalescence occurs. The field of view is 6.8 × 5.1 mm, and the movie is played back at 30× fast-forward.

Movie S5